Available online at www.sciencedirect.com
ScienceDirect
Journal of Sound and Vibration 320 (2009) 496–515
JOURNAL OF SOUND AND VIBRATION
www.elsevier.com/locate/jsvi

A built-in force actuator for active control of lateral rotor vibration in cage induction electrical machines

Antti Laiho[a,*], Kari Tammi[a], Andrej Burakov[b], Antero Arkkio[c], Kai Zenger[c]

[a]VTT Industrial Systems, P.O. Box 13022, FIN-02044 VTT Espoo, Finland
[b]Fortum Service, Hydro- and Windpower Engineering, P.O. Box 100, FIN-00048 FORTUM, Finland
[c]Faculty of Electronics, Communications and Automation, Helsinki University of Technology, FIN-02015 TKK, Finland

Received 14 November 2007; received in revised form 31 July 2008; accepted 4 August 2008
Handling Editor: C.L. Morfey
Available online 1 October 2008

Abstract

In this paper means of active control of radial rotor vibrations in electrical machines are considered. We examine a built-in force actuator for active generation of force on the machine rotor. The operation of the actuator is based on electromechanical interaction between the rotor and the stator of the machine. The actuator is given a low-order linear state-space model, which is identified by using simulation data obtained from a detailed time-stepping finite element model of the machine. Simulation results obtained by using real machine data and finite element time-stepping method are presented.

1. Introduction

In rotating machines vibration is induced by harmonic excitation forces at the rotor rotation speed (unbalanced mass excitation) with higher harmonic components. These low-frequency range vibratory effects are the most important sources of rotor vibration in rotating machinery [1]. Vibration in electrical machines may lead to such problems as noise, increased bearing wear or rotordynamic instability. In induction machines with conventional bearings 42–50% of the faults are bearing related [2]. An increased bearing wear caused by vibration may reduce bearing lifetime considerably. This in turn leads to higher maintenance costs and even expensive process downtime. In addition, rotor vibration puts demands on machine design. Rotating machines are generally designed to operate either at subcritical or supercritical range. Operation close to critical speed is precluded even if there were passive vibration control devices used.

The above-mentioned rotor vibration-induced phenomena could be attenuated by active rotor vibration control. However, the force actuation on the rotor is problematic in some cases because of the actuator installation problems. Indeed, at low-frequency range, in order to attenuate rotor bending vibration, the

*Corresponding author.
E-mail addresses: Antti.Laiho@vtt.fi (A. Laiho), Kari.Tammi@vtt.fi (K. Tammi), Andrej.Burakov@tkk.fi (A. Burakov), Antero.Arkkio@tkk.fi (A. Arkkio), Kai.Zenger@tkk.fi (K. Zenger).

0022-460X/$ - see front matter © 2008 Elsevier Ltd. All rights reserved.
doi:10.1016/j.jsv.2008.08.003

Nomenclature

B	air-gap flux density
$\hat{B}_k$	flux density harmonic k
d_r	rotor core diameter
$f_c, \mathbf{f}_c$	control force
$\mathbf{f}_{\text{ex}}$	excitation force
$\mathscr{F}$	air-gap MMF
$\hat{\mathscr{F}}_k$	MMF harmonic k
$\hat{i}_{r,p\pm1}$	rotor cage current $p \pm 1$ harmonics
$\hat{i}_{c,p+1}$	control winding current
$\mathbf{I}$	unit matrix
$\mathbf{i}$	current vector
j	imaginary unit
$k_{r,p\pm1}$	rotor cage coupling factors
$k_{c,p+1}$	control winding coupling factor
l_r	rotor core length
$L_{c,p+1}$	control winding inductance
L	rotor cage mesh segment inductance
$L_{r,p\pm1}$	rotor cage inductance
$M_{r,c,p+1}$	mutual inductance
p	number of pole-pairs
$R_{c,p+1}$	control winding resistance
$R_{r,p\pm1}$	rotor cage resistance of harmonics $p \pm 1$
t	time
$\hat{U}_{c,p+1}$	control winding voltage
z_r	rotor center position
δ	eccentric-rotor air-gap length
δ_0	effective air-gap length
$\boldsymbol{\eta}$	modal coordinate vector
λ	air-gap permeance
μ_0	permeability of vacuum
$\boldsymbol{\xi}$	modal velocity vector
$\boldsymbol{\Xi}$	modal damping matrix
σ	Maxwell stress tensor
$\boldsymbol{\Phi}_{\text{rc}}$	modal matrix
φ	angular coordinate
$\boldsymbol{\Omega}$	modal stiffness matrix
ω_1	supply frequency
ω_c	control winding supply frequency
ω_m	rotor angular frequency
exp, e	exponential function
X^r	X in rotor coordinates
X^*	complex conjugate of X
$\lvert X \rvert$	absolute value of X
$\dot{X}$	time-derivative of X
$\hat{X}$	space-vector X
$\text{Re}(X)$	real part of X
$\text{Im}(X)$	imaginary part of X
AMB	active magnetic bearing
FE	finite element
FRF	frequency response function
IM	induction machine
LTI	linear time-invariant
MMF	magnetomotive force
UMP	unbalanced magnetic pull

actuator should be installed at the rotor center, which may not be possible in some applications. This fact provokes demands for a built-in force actuator. For instance, in small-power electrical machines, the force actuator based on a supplementary winding design has been used in bearingless machine design [3]. However, in larger flexible-shaft electrical machines conventional journal bearings are still widely used and bearing relief methodology has not been applied.

In this paper, we consider a force actuation methodology proposed for a cage induction motor with conventional bearings. A built-in force actuator based on the electromechanical interaction between the rotor and stator of the machine is examined. In an electrical machine the air-gap magnetic field distortion induces forces on the rotor. The effect is referred to as the unbalanced magnetic pull (UMP) [4–7]. The effect of UMP on electrical machine rotordynamics is that it decreases the critical speeds of the machine and may lead to increased bearing wear or rotordynamic instability [8,9]. The effect of UMP was observed already in early 20th century [10]. In electrical machines the phenomenon has been used for force production in active magnetic bearing (AMB) technology and from early 1990s also in bearingless machine design. Chiba et al. [11] considered a four-pole induction motor to which a supplementary two-pole winding, referred to as 'suspension winding', was constructed. By applying a feedback control system the rotor was balanced by UMP induced by the unbalanced air-gap flux, when current was fed into the suspension winding. Later on, this built-in force actuator was applied for several small-power applications [3,12,13].

In this work, we consider utilization of UMP for active radial rotor vibration control in flexible shaft induction machines with conventional bearings. We consider large induction machines with low critical speed (~20 Hz). Earlier results considering radial rotor vibration attenuation by using a UMP-based force actuator have been reported by S. Watanabe et al. [14]. In the present paper simulation results are presented in which a

two-pole induction machine with squirrel-cage rotor and journal bearings is equipped with a supplementary four-pole winding distributed in the stator slots. Real machine data of a laboratory-scale test motor imitating big electrical motors was used.

In bearingless induction machines the conventional squirrel-cage rotor is not practical [3]. This is because, due to the slip between the supplementary winding field and rotor rotation speed, currents are induced in the rotor cage when the supplementary winding is excited. The problem can be solved by using a pole-specific rotor design [15]. However, in the present work we restrict ourselves to conventional cage rotors and, contrary to suspension methodology, mainly focus on producing circulating force synchronized with the rotor rotation speed.

In this work, we develop a low-order linear time-invariant (LTI) state-space model of the force actuator. The state-space model is obtained through identification procedure from finite element (FE) simulations carried out by using the test machine data. The methodology provides a virtual plant of the machine which can be used in the actuator design in prior to implementing it in a real machine.

2. Methods and system configuration

We consider a p pole-pair induction machine (IM) with a squirrel cage rotor structure. Furthermore, a small $p+1$ pole-pair supplementary winding, referred to as 'control winding', is distributed in the stator slots at the wedge region. In Fig. 1(a) schematic picture of the machine cross-section is shown. In the figure, the notation $\odot$ means that when phase current is positive then current is flowing out of the page while $\otimes$ means that it is flowing into the page. The main winding coils are located at the outer part and the control winding coils at the inner part of each stator slot (see Fig. 1(b)). The winding schema follows the winding diagram given in Table 2. A net force $\mathbf{f}_c$ is exerted on the rotor. The force is induced by the non-symmetric field distribution in the air-gap caused by eccentric rotor motion and currents in two windings.

In the machine cross-section, the magnetic field in the air gap is developed into double Fourier series of two variables; time and the spatial (angular) coordinate along the rotor surface. The air-gap field spatial harmonic with wavenumber k is systematically referred to as 'k (spatial) harmonic' [16]. In the p pole-pair induction machine design the main stator winding is distributed in the stator slots so that it mainly produces p harmonic field in the air-gap but in practice higher order harmonics, referred to as 'slotting harmonics', appear as well.

Similarly, when a 3-phase voltage is supplied to the control winding, a $p+1$ harmonic field component is induced in the air gap. Consequently, due to the non-symmetric air-gap field a net force exerted on the rotor is produced [3]. The force can be actively controlled by a separate frequency converter supplying voltage to the supplementary winding. In addition, eccentric rotor motion produces UMP [17] which contributes to the net force exerted on the rotor.

The low-order actuator-rotor model presented here consists of an electromechanical actuator model, which is coupled with a mechanical model of the rotor consisting of the machine housing, stator, bearings and the

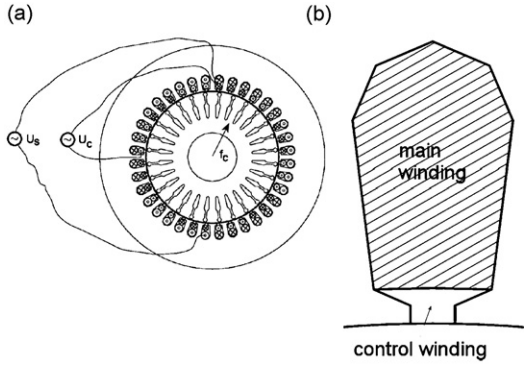

Fig. 1. A cross-section of a two-pole machine to which a four-pole control winding is distributed in the stator slots: (a) machine cross-section showing the main winding with voltage source $\mathbf{U}_s$ and control winding with voltage source $\mathbf{U}_c$ and (b) single stator slot with the control winding coils placed in the wedge region. Further details are given in Section 2.

rotor. The parameters of the low-order model are identified from time-series data obtained from a more detailed FE-based field-circuit analysis of the machine [18,19]. The parameters of the low-order actuator model were identified in the frequency-domain by applying subspace identification [20].

2.1. Force actuator model

In the following, a low-order LTI model of the force actuator is derived. The main assumptions in the analytical derivation of the force actuator model are:

(1) coupling between the control winding and the main stator winding is neglected,
(2) magnetic fields are studied in a transversal two-dimensional machine cross-section where control force is applied. The tangential components of the magnetic fields are neglected,
(3) saturation of the magnetic materials is neglected; linear equations for voltage and flux are used,
(4) stator windings are series connected,
(5) higher harmonic field components are neglected.

The condition of the first assumption can be justified by proper control winding design so that there would be negligible magnetic coupling between the control winding and the field winding. In fact, main winding p harmonic and control winding $p+1$ harmonic are coupled only through the rotor cage and eccentric rotor motion. Constant operational conditions (constant rotation speed, constant flux) are assumed and control winding is assumed not to have effect on the machine operation. Furthermore, three-dimensional effects such as homopolar flux (two-pole machines) and end-winding dynamics are neglected.

In the literature, it is common practice to neglect the tangential air-gap field component, since it is typically noticeably smaller than the radial field component. Moreover, the saturation of magnetic materials brings nonlinearity to the actuator dynamics which was neglected in the modeling. However, linearity of the actuator is examined by simulations carried out by using a more detailed FE analysis including saturation of magnetic materials. This enables choosing an appropriate operation point (control winding input voltage and disturbance force level) for the linear model.

We assume that the stator windings are series connected. Parallel stator connections would affect the net force exerted on the rotor [4]. In the air gap, there are higher harmonic air-gap field spatial harmonics such as stator slotting harmonics, which are neglected in the model. We restrict ourselves to the low-frequency range in the vicinity of the rotor bending flexural modes.

In the following, the space-vector formalism [16] is adopted. Quantities with hat denote complex-valued functions of time (spatial Fourier coefficients) with subindex denoting the harmonic order (spatial wavenumber). The superscript '$*$' denotes complex conjugation. Expressions given in the rotor coordinate system are denoted by superscript 'r'.

The main magnetomotive force (MMF) harmonics in the air-gap are of order p and $p\pm1$. In the following, the other MMF harmonics are neglected. The p harmonic is induced by current in the main winding, $p+1$ by the currents in the control winding and the rotor cage, and $p-1$ is produced by the rotor cage current $p-1$ harmonic. The rotor cage current $p\pm1$ harmonics are induced by the eccentric rotor motion.

In the stator reference frame, the MMF distribution in the air gap at time instant t with angular coordinate φ is given by

$$\mathscr{F}(t,\varphi)=\mathrm{Re}\{\hat{\mathscr{F}}_p(t)\mathrm{e}^{-\mathrm{j}p\varphi}+\hat{\mathscr{F}}_{p-1}(t)\mathrm{e}^{-\mathrm{j}(p-1)\varphi}+\hat{\mathscr{F}}_{p+1}(t)\mathrm{e}^{-\mathrm{j}(p+1)\varphi}\}. \tag{1}$$

In Eq. (1) the subscripts p and $p\pm1$ refer to the corresponding spatial harmonics. In the case $p=1$ the $p-1$-component is neglected which means that the homopolar flux is not taken into consideration for two-pole machines. Furthermore, we have

$$\hat{\mathscr{F}}_p=\hat{\mathscr{F}}_{s,p}+\hat{\mathscr{F}}_{r,p}, \tag{2}$$

$$\hat{\mathscr{F}}_{p-1}=\hat{\mathscr{F}}_{r,p-1}, \tag{3}$$

$$\hat{\mathscr{F}}_{p+1}=\hat{\mathscr{F}}_{c,p+1}+\hat{\mathscr{F}}_{r,p+1}, \tag{4}$$

where $\hat{\mathscr{F}}_{s,p}$ and $\hat{\mathscr{F}}_{r,p}$ are the fundamental MMF waves induced by the currents in the stator windings and rotor cage, respectively, $\hat{\mathscr{F}}_{r,p\pm1}$ is the MMF induced to the air-gap by the rotor cage currents $p\pm1$ and $\hat{\mathscr{F}}_{c,p+1}$ is the MMF produced by control winding current.

The radial magnetic flux density in the air-gap is given by

$$B(t,\varphi)=\lambda(t,\varphi)\mathscr{F}(t,\varphi), \tag{5}$$

where the air-gap permeance is $\lambda(t,\varphi)=\mu_0/\delta(t,\varphi)$ in which the air-gap length δ for (slightly) eccentric rotor at angular position φ is given by

$$\delta(t,\varphi)=\delta_0-\mathrm{Re}\{z_r(t)\mathrm{e}^{-\mathrm{j}\varphi}\}. \tag{6}$$

Here δ_0 is the effective radial air-gap length for the concentric rotor and z_r is the rotor center position in the complex plane (see Fig. 2). The effect of the stator slotting on the air-gap permeance can approximately be taken into account in δ_0. By using the two first terms in Taylor expansion in Eq. (6) we obtain

$$\lambda(t,\varphi)=\mu_0/\delta(t,\varphi)\approx\frac{\mu_0}{\delta_0}\left[1+\frac{1}{\delta_0}\mathrm{Re}\{z_r(t)\mathrm{e}^{-\mathrm{j}\varphi}\}\right]. \tag{7}$$

Consequently, substituting Eqs. (1) and (7) to Eq. (5) gives

$$\begin{aligned}B(t,\varphi)=\frac{\mu_0}{\delta_0}\mathrm{Re}\Bigg\{&\left[\hat{\mathscr{F}}_p+\frac{1}{2\delta_0}(\hat{\mathscr{F}}_{p-1}z_r+\hat{\mathscr{F}}_{p+1}z_r^*)\right]\mathrm{e}^{-\mathrm{j}p\varphi}\\&+\left(\hat{\mathscr{F}}_{p-1}+\frac{1}{2\delta_0}\hat{\mathscr{F}}_p z_r^*\right)\mathrm{e}^{-\mathrm{j}(p-1)\varphi}+\left(\hat{\mathscr{F}}_{p+1}+\frac{1}{2\delta_0}\hat{\mathscr{F}}_p z_r\right)\mathrm{e}^{-\mathrm{j}(p+1)\varphi}\\&+\frac{1}{2\delta_0}\hat{\mathscr{F}}_{p+1}z_r\mathrm{e}^{-\mathrm{j}(p+2)\varphi}+\frac{1}{2\delta_0}\hat{\mathscr{F}}_{p-1}z_r^*\mathrm{e}^{-\mathrm{j}(p-2)\varphi}\Bigg\}.\end{aligned} \tag{8}$$

We assume that the fundamental MMF component $\hat{\mathscr{F}}_p$ dominates the harmonics $\hat{\mathscr{F}}_{p\pm1}$. In addition, we neglect the harmonics $p\pm2$. Under these assumptions, we obtain

$$B(t,\varphi)\approx\mathrm{Re}\{\hat{B}_p\mathrm{e}^{-\mathrm{j}p\varphi}+\hat{B}_{p-1}\mathrm{e}^{-\mathrm{j}(p-1)\varphi}+\hat{B}_{p+1}\mathrm{e}^{-\mathrm{j}(p+1)\varphi}\}, \tag{9}$$

where we have introduced

$$\hat{B}_p=\frac{\mu_0}{\delta_0}\hat{\mathscr{F}}_p, \tag{10}$$

$$\hat{B}_{p-1}=\frac{\mu_0}{\delta_0}\left(\frac{z_r^*}{2\delta_0}\hat{\mathscr{F}}_p+\hat{\mathscr{F}}_{p-1}\right)=\frac{z_r^*}{2\delta_0}\hat{B}_p+\frac{\mu_0}{\delta_0}\hat{\mathscr{F}}_{p-1}, \tag{11}$$

$$\hat{B}_{p+1}=\frac{\mu_0}{\delta_0}\left(\frac{z_r}{2\delta_0}\hat{\mathscr{F}}_p+\hat{\mathscr{F}}_{p+1}\right)=\frac{z_r}{2\delta_0}\hat{B}_p+\frac{\mu_0}{\delta_0}\hat{\mathscr{F}}_{p+1}. \tag{12}$$

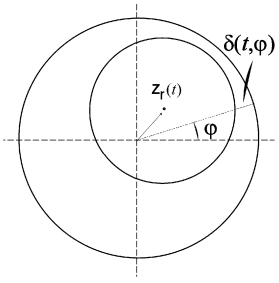

Fig. 2. Eccentric rotor motion modifies the radial air-gap length resulting to non-uniform air-gap field. Here, z_r denotes the rotor center position in the complex plane and φ the angular coordinate in the stator reference frame. Figure is out-of-scale.

In the stator reference frame, the total force exerted on the rotor is given by

$$f_c(t) = \frac{d_r l_r}{2} \int_0^{2\pi} \sigma(t,\varphi) \mathrm{e}^{\mathrm{j}\varphi}\, \mathrm{d}\varphi, \tag{13}$$

where d_r and l_r are the diameter and length of the rotor core, respectively. The radial component of the Maxwell stress tensor is given by

$$\sigma(t,\varphi) = \frac{1}{2\mu_0} B(t,\varphi)^2, \tag{14}$$

where we have approximated the iron core to have infinite permeability, and only the radial magnetic field component was taken into account. From Eq. (13) we obtain

$$\begin{aligned} f_c &= \frac{2\pi d_r l_r}{2} \frac{1}{2\mu_0} \frac{1}{4} (2\hat{B}_p \hat{B}^*_{p-1} + 2\hat{B}^*_p \hat{B}_{p+1}) \\ &= \frac{\pi d_r l_r}{4\mu_0 \delta_0} (|\hat{B}_p|^2 z_r + \mu_0 \hat{B}_p \hat{\mathscr{F}}^*_{p-1} + \mu_0 \hat{B}^*_p \hat{\mathscr{F}}_{p+1}) \\ &= \frac{\pi d_r l_r}{4\mu_0 \delta_0} (|\hat{B}_p|^2 z_r + \mu_0 k_{r,p-1} \hat{B}_p \hat{i}^*_{r,p-1} + \mu_0 k_{r,p+1} \hat{B}^*_p \hat{i}_{r,p+1} + \mu_0 k_{c,p+1} \hat{B}^*_p \hat{i}_{c,p+1}), \end{aligned} \tag{15}$$

where we have used Eqs. (14), (9), (11), (12), (3) and (4). In Eq. (15) we have introduced

$$\hat{\mathscr{F}}_{r,p\pm1} = k_{r,p\pm1} \hat{i}_{r,p\pm1},$$

$$\hat{\mathscr{F}}_{c,p+1} = k_{c,p+1} \hat{i}_{c,p+1},$$

where the space vectors $\hat{i}_{r,p\pm1}$ and $\hat{i}_{c,p+1}$ are for rotor cage current $p \pm 1$ components and control winding current, respectively. The coupling factors $k_{r,p\pm1}$ and $k_{c,p+1}$ measure how effectively the corresponding current components produce MMF. The saturation due to nonlinear magnetic materials is neglected, and formulas are assumed to be given at a specific operation point. In the modeling the rotor cage is replaced by an equivalent 3-phase winding, and space vector theory [21] is applied in the equivalent winding structure. In the case of $p = 1$ the $p - 1$ components are discarded and, consequently, in Eq. (15) $|\hat{B}_p|^2$ is multiplied by $1/2$.

In the induction machine with a supplementary control winding, the control winding input voltage gives rise to the control winding current. As well, the eccentric rotor motion induces $p \pm 1$ currents to the rotor cage [17]. Furthermore, the rotor cage and control winding are magnetically coupled. We apply the induction machine voltage and flux equations [16] for control winding $p + 1$ and rotor cage $p \pm 1$ harmonics. Furthermore, we apply the eccentric rotor cage model [17]. In the model, the eccentric rotor motion acts as a source for the rotor cage harmonic components $p \pm 1$ which, in turn, contribute to UMP. We have

$$\hat{U}_{c,p+1} - M_{r,c,p+1} \frac{\mathrm{d}\hat{i}_{r,p+1}}{\mathrm{d}t} = L_{c,p+1} \frac{\mathrm{d}\hat{i}_{c,p+1}}{\mathrm{d}t} + R_{c,p+1} \hat{i}_{c,p+1}, \tag{16}$$

$$-\frac{L k_{r,p+1}}{2\mu_0} \frac{\mathrm{d}}{\mathrm{d}t} (\hat{B}^r_p z^r_r) - M_{r,c,p+1} \frac{\mathrm{d}\hat{i}^r_{c,p+1}}{\mathrm{d}t} = L_{r,p+1} \frac{\mathrm{d}\hat{i}^r_{r,p+1}}{\mathrm{d}t} + R_{r,p+1} \hat{i}^r_{r,p+1}, \tag{17}$$

$$-\frac{L k_{r,p-1}}{2\mu_0} \frac{\mathrm{d}}{\mathrm{d}t} (\hat{B}^r_p z^{r*}_r) = L_{r,p-1} \frac{\mathrm{d}\hat{i}^r_{r,p-1}}{\mathrm{d}t} + R_{r,p-1} \hat{i}^r_{r,p-1}. \tag{18}$$

In Eq. (16) we have introduced the $p + 1$ harmonic components $\hat{U}_{c,p+1}$, $L_{c,p+1}$, $R_{c,p+1}$ and $M_{r,c,p+1}$ which stand for the control winding input voltage, control winding inductance, control winding resistance and mutual inductance between the rotor cage and the control winding, respectively. In Eqs. (17) and (18) the upper index 'r' refers to the rotor reference frame which is rotating at the mechanical rotation angular velocity ω_m with respect to the stator reference frame. Furthermore, we have introduced L denoting the self-inductance of a single rotor cage loop consisting of two rotor bars and end-ring segments between them, $L_{r,p\pm1}$ the rotor cage $p \pm 1$ inductance and $R_{r,p\pm1}$ the rotor cage $p \pm 1$ resistance [17].

In Eqs. (16)–(18) we have neglected the rotor cage current $p+2$ and p harmonics. The harmonic $p+2$ is produced by the eccentric rotor motion with respect to the control winding and is given by an equation similar to Eq. (18). However, the air-gap field induced by the control winding is negligible compared to the one induced by the main winding and hence the $p+2$ currents can be neglected. The p harmonic current is induced in the rotor cage by the main winding current and eccentric rotor motion with respect to the control winding. Here, the component induced by the eccentric rotor motion with respect to the control winding was neglected. In the constant-flux operation conditions, we have

$$\hat{B}_p = B_p \mathrm{e}^{\mathrm{j}\omega_1 t} \tag{19}$$

in which ω_1 is the main winding supply frequency (rad/s) and B_p is the constant complex amplitude of the fundamental field component. Substitution of Eq. (19) to Eq. (15) leads to time-variant force expression which precludes LTI formulation. Indeed, from Eqs. (15)–(18) we see that, for concentric rotor ($z_r = 0$), the non-zero current terms $\hat{i}_{c,p+1}$ and $\hat{i}_{r,p+1}$ are modulated by $\exp(-\mathrm{j}\omega_1 t)$ which means that a DC control winding input voltage creates a rotating actuator force with angular velocity $-\omega_1$ (clockwise direction). In order to obtain an LTI system we introduce

$$\hat{i}_{r,p\pm1,0} = \hat{i}_{r,p\pm1} \mathrm{e}^{-\mathrm{j}\omega_1 t}, \tag{20}$$

$$\hat{i}_{c,p+1,0} = \hat{i}_{c,p+1} \mathrm{e}^{-\mathrm{j}\omega_1 t}. \tag{21}$$

We substitute Eq. (19) and Eqs. (20) and (21) in Eq. (15) and obtain the force f_c as a linear combination of the rotor position and the current terms, in which the coefficients are time-independent which gives rise to LTI system. Furthermore, Eqs. (20) and (21) are substituted in Eq. (16) with

$$\hat{U}_{c,p+1,0} = \hat{U}_{c,p+1} \mathrm{e}^{-\mathrm{j}\omega_1 t}. \tag{22}$$

The expressions given by Eqs. (17) and (18) are given in the rotor reference frame rotating at angular velocity ω_m with respect to the stator reference frame. We have the relations

$$\hat{i}^r_{c,p+1} = \hat{i}_{c,p+1} \mathrm{e}^{-\mathrm{j}(p+1)\omega_m t} = \hat{i}_{c,p+1,0} \mathrm{e}^{\mathrm{j}(\omega_1-(p+1)\omega_m)t} = \hat{i}_{c,p+1,0} \mathrm{e}^{\mathrm{j}\omega_{p+1} t}, \tag{23}$$

$$\hat{i}^r_{r,p\pm1} = \hat{i}_{r,p\pm1} \mathrm{e}^{-\mathrm{j}(p\pm1)\omega_m t} = \hat{i}_{r,p\pm1,0} \mathrm{e}^{\mathrm{j}(\omega_1-(p\pm1)\omega_m)t} = \hat{i}_{r,p\pm1,0} \mathrm{e}^{\mathrm{j}\omega_{p\pm1} t}, \tag{24}$$

$$z^r_r = z_r \mathrm{e}^{-\mathrm{j}\omega_m t}. \tag{25}$$

We substitute Eqs. (23)–(25) with

$$\hat{B}^r_p = \hat{B}_p \mathrm{e}^{-\mathrm{j}p\omega_m t} = B_p \mathrm{e}^{\mathrm{j}(\omega_1 - p\omega_m)t} \tag{26}$$

in Eqs. (17) and (18). Finally, we obtain the system

$$f_c = \frac{\pi d_r l_r}{4\mu_0 \delta_0} (|\hat{B}_p|^2 z_r + \mu_0 k_{r,p-1} B_p \hat{i}^*_{r,p-1,0} + \mu_0 k_{r,p+1} B^*_p \hat{i}_{r,p+1,0} + \mu_0 k_{c,p+1} B^*_p \hat{i}_{c,p+1,0}), \tag{27}$$

$$\hat{U}_{c,p+1,0} = (R_{c,p+1} + \mathrm{j}\omega_1 L_{c,p+1}) \hat{i}_{c,p+1,0} + \mathrm{j}\omega_1 M_{r,c,p+1} \hat{i}_{r,p+1,0} + M_{r,c,p+1} \frac{\mathrm{d}\hat{i}_{r,p+1,0}}{\mathrm{d}t} + L_{c,p+1} \frac{\mathrm{d}\hat{i}_{c,p+1,0}}{\mathrm{d}t}, \tag{28}$$

$$\begin{aligned} &L_{r,p+1} \frac{\mathrm{d}\hat{i}_{r,p+1,0}}{\mathrm{d}t} + (R_{r,p+1} + \mathrm{j}\omega_{p+1} L_{r,p+1}) \hat{i}_{r,p+1,0} + \mathrm{j}\omega_{p+1} M_{r,c,p+1} \hat{i}_{c,p+1,0} \\ &\quad + M_{r,c,p+1} \frac{\mathrm{d}\hat{i}_{c,p+1,0}}{\mathrm{d}t} + \frac{L k_{r,p+1}}{2\mu_0} B_p (\dot{z}_r + \mathrm{j}\omega_{p+1} z_r) = 0, \end{aligned} \tag{29}$$

$$L_{r,p-1} \frac{\mathrm{d}\hat{i}^*_{r,p-1,0}}{\mathrm{d}t} + (R_{r,p-1} - \mathrm{j}\omega_{p-1} L_{r,p-1}) \hat{i}^*_{r,p-1,0} + \frac{L k_{r,p-1}}{2\mu_0} B^*_p (\dot{z}_r - \mathrm{j}\omega_{p-1} z_r) = 0. \tag{30}$$

The voltage $\hat{U}_{c,p+1,0}$ fed to the control winding gives rise to a control winding current given by Eq. (28). The rotor cage and control winding are coupled by mutual inductance $M_{r,c,p+1}$ in Eqs. (28) and (29). Furthermore,

the eccentric rotor motion induces rotor cage currents along with Eqs. (29) and (30). Hence, the force exerted on the rotor is given by Eq. (27) as a weighted sum of the rotor eccentricity and induced rotor cage and control winding currents. From Eqs. (27), (28) and (22) we see that when a 3-phase voltage of frequency ω_c is supplied to the control winding, the resulting force f_c rotates with angular frequency $\omega_c - \omega_1$ in the stator reference frame.

The system given by Eqs. (27)–(30) can be re-written as a real-valued LTI system given by

$$\frac{\mathrm{d}\mathbf{i}}{\mathrm{d}t} = \mathbf{A}_{\mathrm{em}}\mathbf{i} + \mathbf{B}_{\mathrm{em}}\mathbf{v} + \mathbf{S}_{\mathrm{em}}\dot{\mathbf{u}}_{\mathrm{rc}} + \mathbf{Q}_{\mathrm{em}}\mathbf{u}_{\mathrm{rc}}, \tag{31}$$

$$\mathbf{f}_c = \mathbf{C}_{\mathrm{em}}\mathbf{i} + \mathbf{P}_{\mathrm{em}}\mathbf{u}_{\mathrm{rc}}, \tag{32}$$

where

$$\mathbf{i} = \begin{pmatrix} \mathrm{Re}\{\hat{i}_{c,p+1,0}\} \\ \mathrm{Re}\{\hat{i}^*_{r,p-1,0}\} \\ \mathrm{Re}\{\hat{i}_{r,p+1,0}\} \\ \mathrm{Im}\{\hat{i}_{c,p+1,0}\} \\ \mathrm{Im}\{\hat{i}^*_{r,p-1,0}\} \\ \mathrm{Im}\{\hat{i}_{r,p+1,0}\} \end{pmatrix} \quad \text{and} \quad \mathbf{v} = \begin{pmatrix} \mathrm{Re}\{\hat{U}_{c,p+1,0}\} \\ \mathrm{Im}\{\hat{U}_{c,p+1,0}\} \end{pmatrix} \tag{33}$$

and $\mathbf{u}_{\mathrm{rc}}$ denotes the rotor center position given by $\mathbf{u}_{\mathrm{rc}} = (\mathrm{Re}\{z_r\}, \mathrm{Im}\{z_r\})^{\mathrm{T}}$. The actuator force vector is given by $\mathbf{f}_c = (\mathrm{Re}\{f_c\}, \mathrm{Im}\{f_c\})^{\mathrm{T}}$. The entries of the real system matrices $\mathbf{A}_{\mathrm{em}}$, $\mathbf{B}_{\mathrm{em}}$, $\mathbf{C}_{\mathrm{em}}$, $\mathbf{S}_{\mathrm{em}}$, $\mathbf{Q}_{\mathrm{em}}$ and $\mathbf{P}_{\mathrm{em}}$ are identified by the means presented later in the text.

2.2. Mechanical model

The mechanical model of the machine consists of structural FE models of the rotor, bearings, stator and the housing. We have neglected the gyroscopic effects and concentrate on the rotor bending flexural vibration modes. However, without loss of generality, the gyroscopic effects can be included in the model by using gyroscopic disks distributed on the rotor shaft [1]. The system order reduction [22] is carried out by solving the n lowest mass-normalized mode shapes and the eigenfrequencies. The reduced-order mechanical model of the electrical machine is hence given by

$$\ddot{\boldsymbol{\eta}} + 2\boldsymbol{\Xi}\boldsymbol{\Omega}\dot{\boldsymbol{\eta}} + \boldsymbol{\Omega}^2\boldsymbol{\eta} = \boldsymbol{\Phi}_{\mathrm{rc}}^{\mathrm{T}}\mathbf{f}_c + \boldsymbol{\Phi}_{\mathrm{rc}}^{\mathrm{T}}\mathbf{f}_{\mathrm{ex}}, \tag{34}$$

$$\mathbf{u}_{\mathrm{rc}} = \boldsymbol{\Phi}_{\mathrm{rc}}\boldsymbol{\eta}, \tag{35}$$

where $\boldsymbol{\eta}$ denotes the modal coordinate vector and

$$\boldsymbol{\Omega} = 2\pi\,\mathrm{diag}\{f_1, \ldots, f_n\},$$

$$\boldsymbol{\Phi} = \{\boldsymbol{\phi}^{(1)}, \ldots, \boldsymbol{\phi}^{(n)}\},$$

$$\boldsymbol{\Xi} = \mathrm{diag}\{\zeta_1, \ldots, \zeta_n\}$$

with f_k denoting the kth eigenfrequency of the machine, $\boldsymbol{\phi}^{(k)}$ the corresponding mass-normalized modal vector and ζ_k the equivalent viscous damping coefficient. In a practical application, the damping coefficients are evaluated by modal testing. In Eq. (34) $\boldsymbol{\Phi}_{\mathrm{rc}}$ denotes the submatrix of $\boldsymbol{\Phi}$ containing the transversal displacement degrees of freedom at the rotor center. The rotor excitation is composed of the control actuator force, $\mathbf{f}_c$, and the disturbance force $\mathbf{f}_{\mathrm{ex}}$ which is dominated by the mass unbalance excitation.

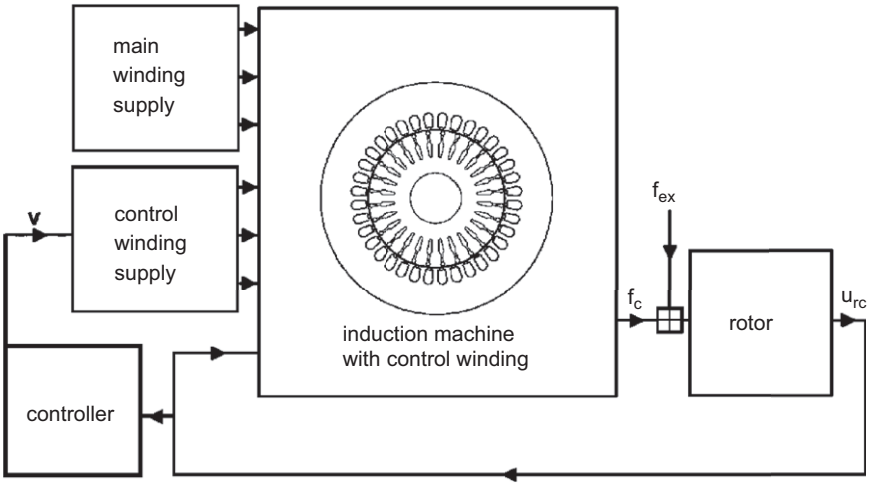

Fig. 3. A schematic view of the induction machine with control winding construction acting as a built-in force actuator. Further details are given in Section 2.3.

2.3. Combined electromechanical system

The electromechanical actuator-rotor system is depicted in Fig. 3. The system inputs are the voltage $\mathbf{v}$ fed to the control winding and the disturbance force $\mathbf{f}_{\mathrm{ex}}$. The control force $\mathbf{f}_c$ given by the actuator and disturbance force $\mathbf{f}_{\mathrm{ex}}$ are exerted to the machine rotor which results to the rotor center displacement $\mathbf{u}_{\mathrm{rc}}$.

The model of the system is obtained by combining the actuator model given by Eqs. (31) and (32) with the structural mechanics model given by Eqs. (34) and (35). As a result, we obtain an electromechanical model of the machine equipped with a force actuator. Indeed, we obtain

$$\frac{\mathrm{d}}{\mathrm{d}t}\begin{pmatrix}\boldsymbol{\xi}\\ \boldsymbol{\eta}\\ \mathbf{i}\end{pmatrix} = \left[\begin{array}{c|c|c} -2\boldsymbol{\Omega}\boldsymbol{\Xi} & \boldsymbol{\Phi}_{\mathrm{rc}}^{\mathrm{T}}\mathbf{P}_{\mathrm{em}}\boldsymbol{\Phi}_{\mathrm{rc}} - \boldsymbol{\Omega}^2 & \boldsymbol{\Phi}_{\mathrm{rc}}^{\mathrm{T}}\mathbf{C}_{\mathrm{em}} \\ \hline \mathbf{I} & \mathbf{0} & \mathbf{0} \\ \hline \mathbf{S}_{\mathrm{em}}\boldsymbol{\Phi}_{\mathrm{rc}} & \mathbf{Q}_{\mathrm{em}}\boldsymbol{\Phi}_{\mathrm{rc}} & \mathbf{A}_{\mathrm{em}} \end{array}\right]\begin{pmatrix}\boldsymbol{\xi}\\ \boldsymbol{\eta}\\ \mathbf{i}\end{pmatrix} + \begin{bmatrix}\mathbf{0}\\ \mathbf{0}\\ \mathbf{B}_{\mathrm{em}}\end{bmatrix}\mathbf{v} + \begin{bmatrix}\boldsymbol{\Phi}_{\mathrm{rc}}^{\mathrm{T}}\\ \mathbf{0}\\ \mathbf{0}\end{bmatrix}\mathbf{f}_{\mathrm{ex}} \tag{36}$$

$$\mathbf{u}_{\mathrm{rc}} = [\mathbf{0}\ \ \boldsymbol{\Phi}_{\mathrm{rc}}\ \ \mathbf{0}]\begin{pmatrix}\boldsymbol{\xi}\\ \boldsymbol{\eta}\\ \mathbf{i}\end{pmatrix}. \tag{37}$$

In the model the inputs to the system are the voltage input $\mathbf{v}$ to the control winding and the disturbance force excitation $\mathbf{f}_{\mathrm{ex}}$ (see Fig. 3). The disturbance mainly consists of the rotation speed harmonics due to the mass unbalance. The voltage $\mathbf{v}$ is the control signal given by the controller and realized by the frequency converter. If the control winding is open the system reduces to the UMP model [23].

The LTI system given by Eqs. (36) and (37) has $2n+6$ ($2n+4$ for a two-pole machine) states where n denotes the number of rotor vibration modes included in the mechanical model. The system has the rotor center displacement $\mathbf{u}_{\mathrm{rc}}$ as an output. In practice, the rotor center displacement is difficult to measure with traditional vibration sensors due to the small air-gap between the rotor and stator. However, in the low-frequency range, the rotor displacement can be measured outside the bearing span resulting in a non-collocated system.

Table 1
Main parameters of the laboratory-scale test machine

Parameter	Value
Supply frequency [Hz]	50
Rated voltage (rms) [V]	400
Connection	delta
Rated current [A]	50
Rated power [kW]	30
Number of phases	3
Number of parallel paths	1
Number of poles	2
Number of stator slots	36
Rated slip [%]	1.0
Rotor mass (rotor core and shaft) [kg]	55.80
Rotor shaft length [mm]	1560
Bearing vertical stiffness [MN/m]	500
Bearing horizontal stiffness [MN/m]	100
Radial air-gap length [mm]	1.0
Critical speed [Hz]	42.0
Nominal speed [Hz]	49.5

Table 2
Winding diagram of the test machine. Capital letters 'A', 'B' and 'C' refer to the phases of the main winding and 'Ac', 'Bc' and 'Cc' refer to the corresponding control winding phase windings

1	2	3	4	5	6	7	8	9	10
−A	−A	−A	−A	−A	−A	+C	+C	+C	+C
−Ac	−Ac	−Ac	+Cc	+Cc	+Cc	−Bc	−Bc	−Bc	+Ac
11	12	13	14	15	16	17	18	19	20
+C	+C	−B	−B	−B	−B	−B	−B	+A	+A
+Ac	+Ac	−Cc	−Cc	−Cc	+Bc	+Bc	+Bc	−Ac	−Ac
21	22	23	24	25	26	27	28	29	30
+A	+A	+A	+A	−C	−C	−C	−C	−C	−C
−Ac	+Cc	+Cc	+Cc	−Bc	−Bc	−Bc	+Ac	+Ac	+Ac
31	32	33	34	35	36				
+B	+B	+B	+B	+B	+B				
−Cc	−Cc	−Cc	+Bc	+Bc	+Bc				

The positive and negative coil sides of the phase windings are denoted by '+' and '−' signs, respectively.

3. Results

The force actuator simulations were carried out for a small 30 kW two-pole cage induction motor. The two-pole machine was chosen due to the fact that they are commonly used in large applications were vibration problems are known to occur. The real machine parameters used in the simulations are listed in Table 1. Specifications of a future laboratory-scale test machine were used. The test machine was designed to imitate a big induction machine. The machine has an extended rotor shaft which brings the critical speed (42.0 Hz) close to the rated speed (49.5 Hz). Winding schema of the machine is given in Table 2. A four-pole winding with 40 turns in each phase is distributed in the stator slots to build the control winding.

The simulations were carried out by using an in-house FE software. In fact, the coupled field-circuit equations were solved in machine cross-section by Crank–Nicholson time-stepping FE analysis [18]. The FE mesh with 4400

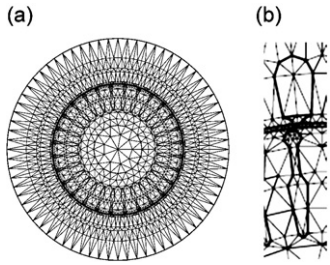

Fig. 4. The FE mesh used in the simulations: (a) mesh consists of 4400 linear triangular elements with 2765 nodes and (b) section of the mesh showing a single stator and rotor slot with air-gap region.

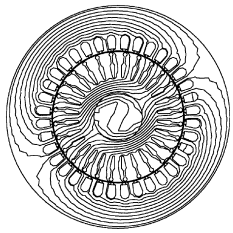

Fig. 5. FE field solution with zero control winding input. The flux between the potential curves is 4.15 mWb/m.

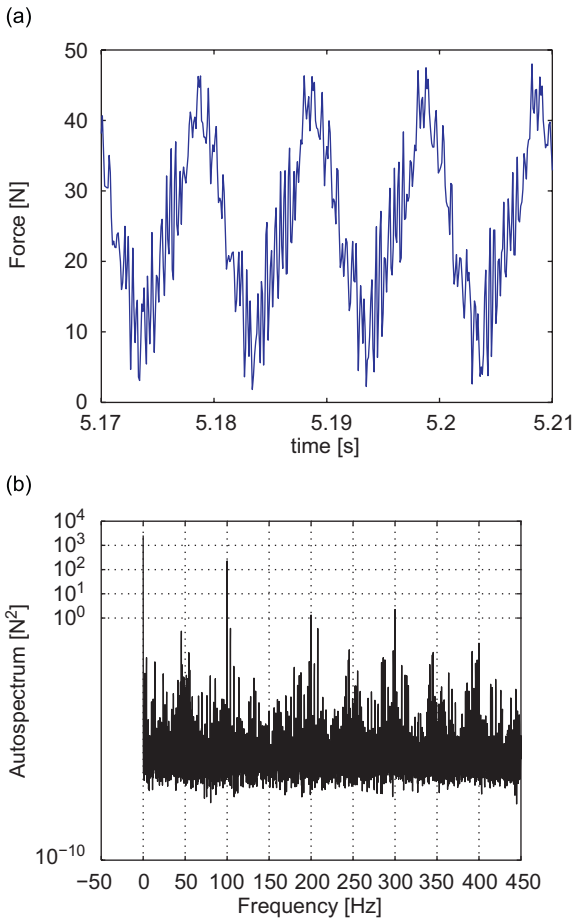

Fig. 6. Horizontal UMP under static eccentricity of 100 μm in the horizontal direction without control winding input: (a) time data and (b) autospectrum of the UMP force. Results from FE analysis.

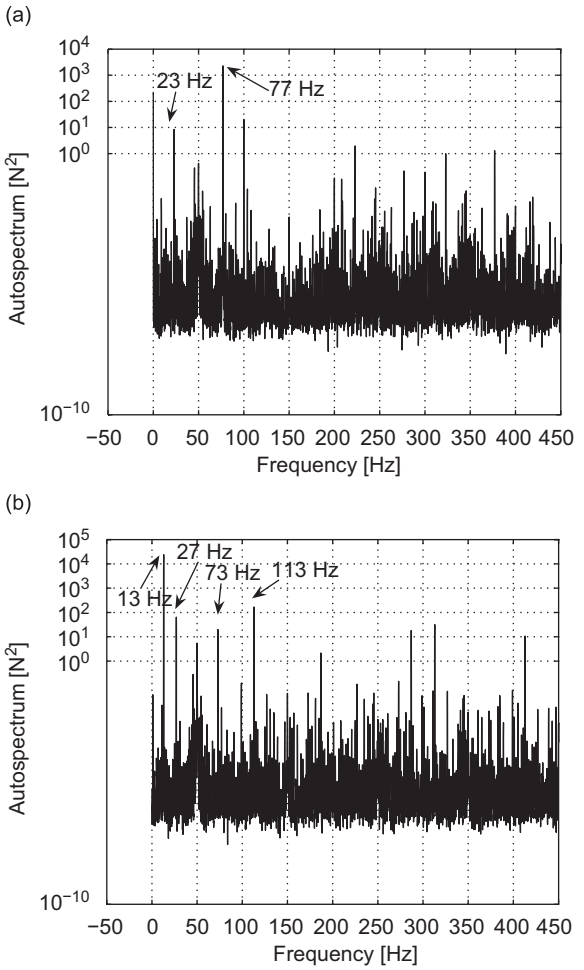

Fig. 7. Autospectrum of actuator force with control winding input and rotor movement: (a) static eccentricity 30 μm, control winding input 127 Hz and 10 V and (b) rotor whirling amplitude 30 μm, whirling frequency 27 Hz, control winding input 37 Hz, 10 V. Results from FE analysis.

linear triangular elements and 2765 nodes is shown in Fig. 4. The transient FE analysis adaptively refines the mesh along with the rotor motion at every time-step. Nonlinear magnetic materials were used in the simulations in order to examine the influence of saturation of the magnetic materials on the actuator force and, on the other hand, to choose the operation point for linearization. Furthermore, detailed stator slot meshing was used in order to bring out the effect of the higher air-gap field harmonics. The effect of end-windings was taken into account by including end-winding impedances in the circuit equations. The control winding was taken into account by additional circuit equations which were embedded in the field-circuit FE model.

The mechanical rotor model was obtained from a commercial FE structural analysis software. The rotor shaft of the test machine was designed so that it would have critical speed at 42.0 Hz. The two lowest rotor modes, i.e. the first flexural rotor bending modes at 42.0 Hz (horizontal rotor bending mode) and 42.3 Hz (vertical rotor bending mode) were included to the modal superposition. The higher rotor bending modes were above 550 Hz and were assumed not to have contribution on the low-frequency behavior of the rotor. The modes were given modal damping of 3% each.

The field-circuit FE analysis software was encoded into a SIMULINK block [19] and connected to the LTI block of the mechanical rotor model (see Fig. 3). A balanced 3-phase voltage of 400 V (rms) and 50 Hz was supplied to the main stator winding. In order to identify the LTI model given by Eqs. (36) and (37), the control winding input voltage was modulated by the supply frequency $\omega_1 = 50$ Hz along with Eq. (22). The input voltage was then transformed to a balanced 3-phase voltage by 2-phase to 3-phase transformation [21].

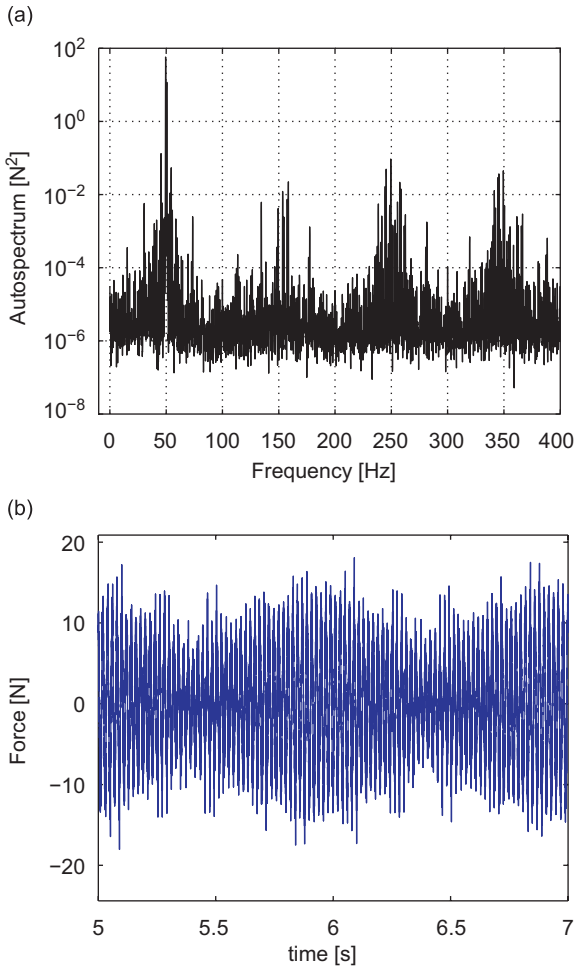

Fig. 8. Horizontal UMP component under synchronous whirling when the rotor is subjected to an unbalanced mass excitation: (a) autospectrum and (b) force versus time. Results from FE analysis.

The real-valued system matrices presented in Eqs. (36) and (37) were identified by using the time-stepping field-circuit FE analysis [18,19] in SIMULINK (see Fig. 3). Indeed, we applied impulse inputs to $\mathbf{v}$ and $\mathbf{f}_{ex}$ resulting to output $\mathbf{u}_{rc}$ which was recorded. The time-step of the simulation was chosen so that a single stator slot is passed by within 6 steps when rotor speed is 49.5 Hz. This gave a time-step of 100 μs. An initial state for the simulation was obtained from the time-harmonic analysis [18]. The steady-state operation at constant speed was determined by carrying out a simulation with zero control-winding input voltage. The steady-state solution was used as an initial state for simulations with control winding voltage input. Hence, the identification was carried out in the frequency-domain by utilizing the subspace identification for linear systems [20]. As a result we obtained the continuous time state space model Eqs. (36) and (37) system matrices.

In Fig. 5 equipotential curves of the magnetic vector potential are depicted showing the two-pole field generated by the main winding under constant rotation speed operational conditions. The field solution was used as an initial state for the control winding input simulations.

3.1. Force actuator dynamics

The actuator dynamics is characterized by control windings combined with UMP induced by the eccentric rotor motion. In the case of static eccentricity without control winding load ($\mathbf{u}_{rc}$ is constant and $\mathbf{v} = \mathbf{0}$) we see from Eqs. (31) and (32) that the model predicts only a static UMP component. However, there are other UMP

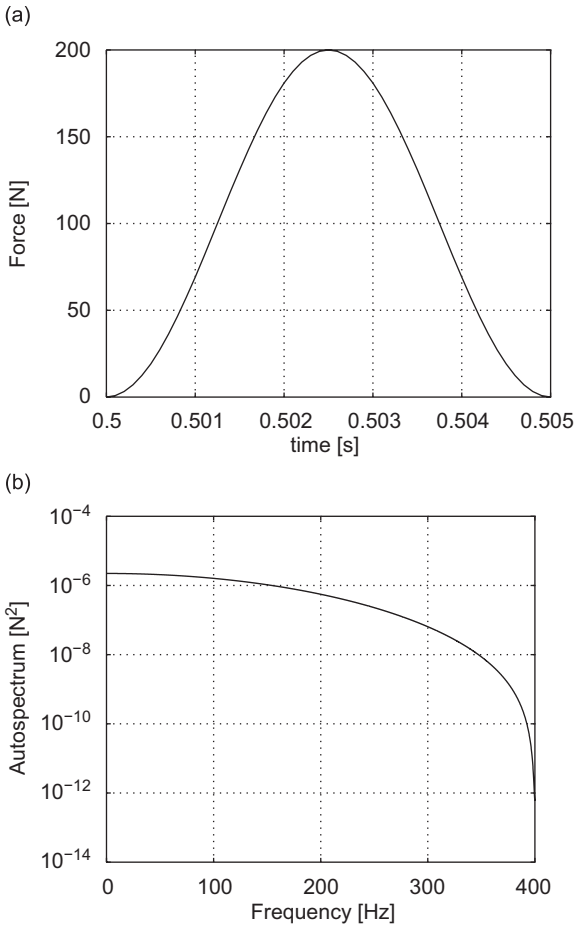

Fig. 9. The force excitation impulse used in the identification: (a) maximum force 200 N starting at 0.5 s and lasting 5 ms and (b) spectrum of the force signal with cut-off at 400 Hz.

harmonics present, as well. The spectrum of UMP is dominated by peaks at 0 Hz and $2\omega_1$ [5,7]. In Fig. 6 the UMP is depicted when there is no control winding supply. The results from FE analysis show that along with the results [5,7] the UMP is dominated by 0 and 100 Hz peaks. From the force autospectrum given in Fig. 6(b) we see that the static term dominates the $2\omega_1 = 100$ Hz peak. However, from the time-series data in Fig. 6(a) we see that the 100 Hz force component has a considerable contribution to UMP.

When the control winding is excited by the symmetrical three-phase voltage with frequency ω_c and the rotor is subjected to static eccentricity, the model given by Eqs. (31) and (32) predicts an actuator force rotating at frequency $\omega_c - \omega_1$ in stator reference frame. In Fig. 7(a) the autospectrum of the actuator force is depicted with control winding load at $\omega_c = 127$ Hz, 10 V and with static eccentricity of 30 μm. The dominating peak is $\omega_c - \omega_1 = 77$ Hz, which dominates the $\omega_c - 3\omega_1 = -23$ Hz and the peaks induced by the eccentricity, 0 Hz and $2\omega_1 = 100$ Hz.

In Fig. 7(b) the autospectrum of the actuator force is depicted with control winding load $\omega_c = 37$ Hz, 10 V and with rotor whirling of amplitude 30 μm and frequency $\omega_w = 27$ Hz. The dominating peak is, as in the static eccentricity case in Fig. 7(a), $\omega_c - \omega_1 = -13$ Hz (actuator force rotating in negative direction, i.e. clockwise) which dominates the minor peaks $\omega_c - 3\omega_1 = -113$ Hz, $2\omega_1 - \omega_w = 73$ Hz and $\omega_w = 27$ Hz.

In Fig. 8 the horizontal UMP component is depicted when the rotor is subjected to an unbalanced mass excitation. The unbalanced mass excitation force was chosen in order to achieve ISO 1940 G2.5 quality grade [24] for rotor balancing. This is, a maximum vibration level of 2.5 mm/s in bearings is allowed. The G2.5 limit gives a 43.4 N unbalanced mass excitation force at rotation frequency 49.5 Hz with the rotor mass 55.8 kg.

The dominant peak in Fig. 8(a) is 49.5 Hz which is the synchronous whirling frequency. In Fig. 8(b) the horizontal UMP after transients is depicted giving a maximum UMP force of 15.0 N. Based on FE simulations carried out for the test machine we see that UMP in synchronous whirling is strongly dominated by the synchronous whirling frequency peak leaving other low-frequency effects as minor ones.

The results obtained from the force actuator simulations motivate that at the low-frequency range the UMP is mainly produced by the control winding supply and the rotor eccentricity is a secondary effect in the actuator dynamics.

3.2. Identification

The force actuator model given by Eqs. (36) and (37) was identified by applying impulse excitations to $\mathbf{f}_{ex}$ and $\mathbf{v}$ and recording the rotor center displacement $\mathbf{u}_{rc}$ as output. This is, the system has 4 inputs and 2 outputs. First, the simulation was run 0.5 s in order to get rid of transients. Then an impulse of the type in Fig. 9(a) was applied. The peak values for the force and voltage impulses were 200 N and 10 V, respectively. The length of the pulse was 5 ms. The cut-off frequency of the excitations was 400 Hz as can be seen from the spectrum in Fig. 9(b). In Fig. 10 simulated typical responses to these impulse excitations are shown. The time-stepping time data was collected for 20 s which gave a frequency resolution of 0.1 Hz including windowing with 90% overlapping and 11 averages. The data sampling frequency was 1 kHz which is easily reachable for commonly

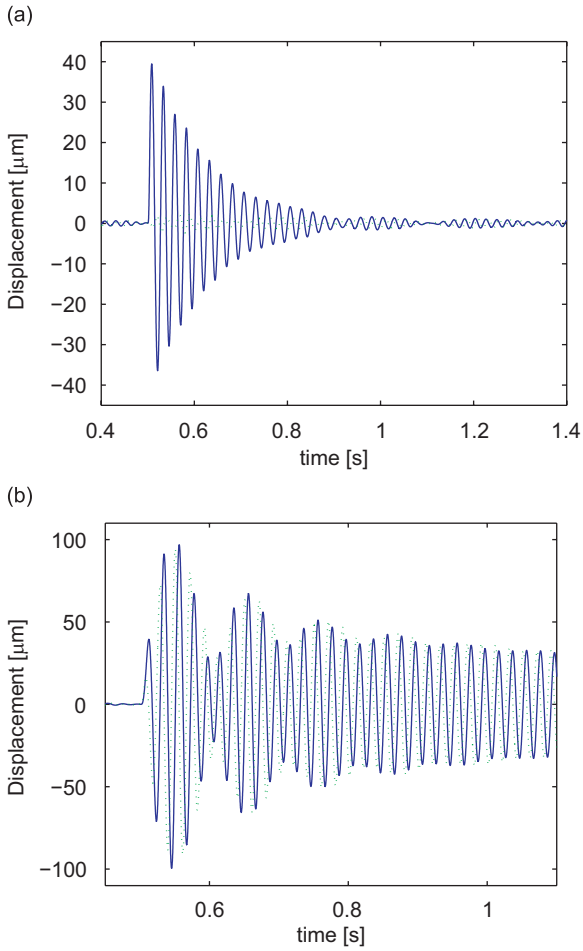

Fig. 10. Rotor center horizontal displacement as response to the impulse excitation: (a) horizontal force impulse of 200 N and (b) control winding voltage impulse of 10 V. - - - -, vertical displacement: —, horizontal displacement. Results from FE analysis.

used frequency converters. The identification was carried out in the frequency-domain by utilizing the subspace identification for linear systems [20].

The linearity of the system was studied by calculating frequency response functions (FRFs) at various input parameter intensities. In Fig. 11 the FRFs with input voltage 2 and 30 V are shown. In Fig. 12 the FRFs from the horizontal excitation force to horizontal and vertical rotor displacements with excitation force level 40 and 600 N (corresponding to the rotor mass 55.8 kg from Table 1) are shown. In Fig. 12(a) the resonance peak is at 40.5 Hz. This differs from the mechanical model resonances at 42.0 Hz due to UMP. In Table 3 the calculated FRFs are compared at various input voltage and excitation force levels. The FRFs from the first input voltage component and horizontal force to the horizontal displacement are considered. The system from the input voltage to the displacement seems to be surprisingly linear at the voltage levels considered [25]. The system from the excitation force shows a bit more nonlinear behavior. A small input force level of 20 N brings considerable amount of disturbances from slotting harmonics, for instance. Identification with a 40 N force input gives a 20.0% higher response level at the resonance compared to the 600 N level. The results shown in Fig. 12(b) declare a small amount of horizontal force to vertical displacement cross-coupling in the system. A lower input force level results in more noisy identification data.

In the identification, a 10th order state-space LTI model was obtained from the subspace identification procedure [20]. The LTI model was hence examined against the field-circuit FE model by comparing FRFs calculated from both the models. In Figs. 13 and 14 the identification results are depicted. In Fig. 13(a) and (b)

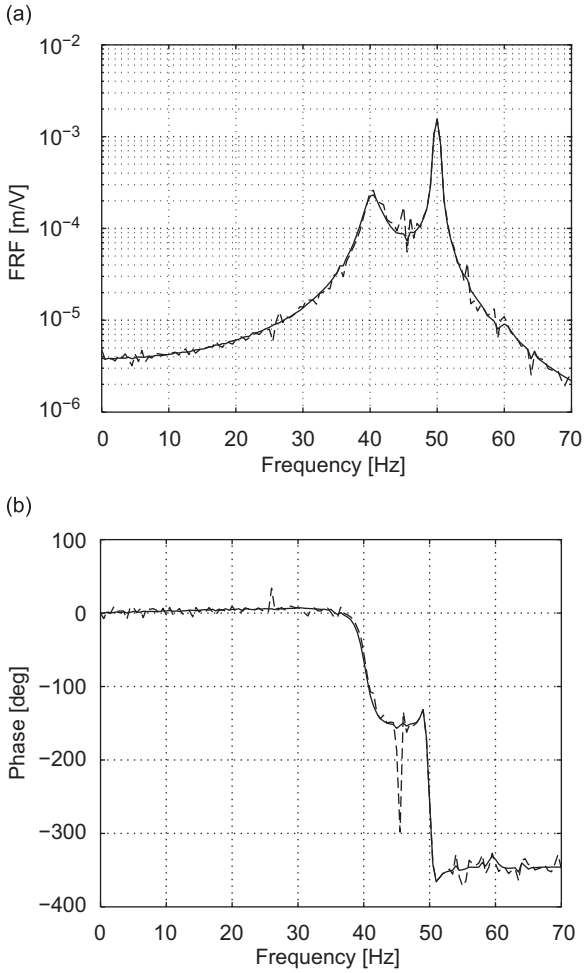

Fig. 11. Frequency response functions from the input voltage first component to horizontal displacement: (a) magnitude and (b) phase. - · · · -, 2 V, —; 30 V.

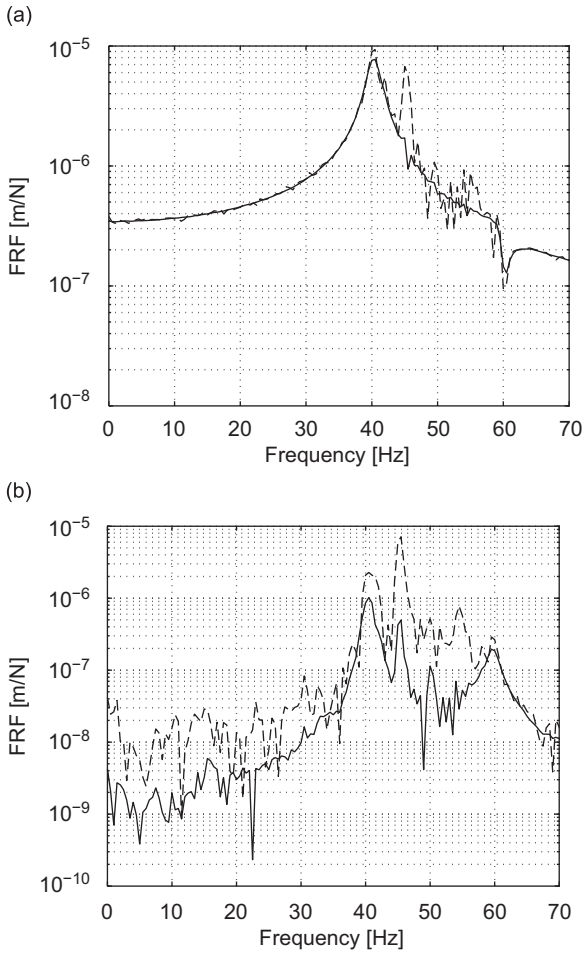

Fig. 12. Frequency responses from the horizontal disturbance force to the rotor center displacement: (a) horizontal displacement and (b) vertical displacement. - · - · -, 40 N; —, 600 N.

Table 3
Frequency response peak values from the horizontal disturbance force and the first component of the control winding input voltage to the horizontal rotor center displacement

Voltage [V]	FRF peak value [μm/mV] (50.0 Hz)	Force [N]	FRF peak value [μm/N] (40.5 Hz)
1	1.549	20	10.95
2	1.54	40	9.326
5	1.535	100	8.352
10	1.534	200	7.958
30	1.535	600	7.734

The peak values are located at 50.0 and 40.5 Hz for the voltage and force input, respectively.

a direct force–displacement FRF is depicted. The mechanical resonance at 42.0 Hz (horizontal bending mode) is shifted to 40.5 Hz which is because of UMP. In Fig. 13(c) and (d) the cross-coupling dynamics stemming from UMP can be observed. The cross-coupling dynamics is much weaker than the direct coupling which can be seen by comparing Fig. 13(a) and (c). However, the cross-coupling is affected by noise which can also be seen by comparing Fig. 13(a) and (c).

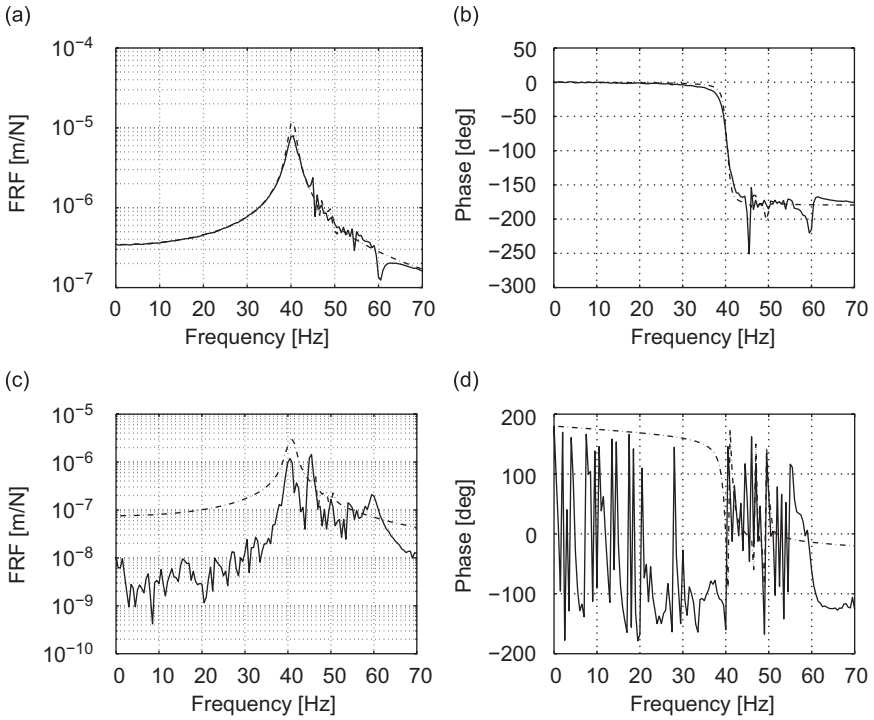

Fig. 13. Identification results of the actuator model from the disturbance force excitation to displacement: (a) horizontal force to horizontal displacement FRF magnitude, (b) horizontal force to horizontal displacement phase, (c) horizontal force to vertical displacement FRF magnitude and (d) horizontal force to vertical displacement phase. —, the simulated FRF; - - -, the identified model FRF. The data was sampled at 1 kHz and the order of the identified LTI model was 10.

In Fig. 14 the FRFs from the control winding input voltage to horizontal and vertical rotor center displacements are shown. The results predict that the actuator has a sharp resonance peak at 50.0 Hz. This can also be seen from the impulse response shown in Fig. 10(b) in which a slowly decaying 50.0 Hz vibration component can be distinguished. The mechanical rotor bending resonance is shifted to 40.5 Hz due to the effect of UMP. The simulated FRFs are close to those obtained from the identified LTI model in the vicinity of the rotation speed. However, at a higher frequency range, the phase error increases as can be seen from Fig. 14(b) and (d).

4. Discussion and conclusions

In this work we presented a force actuator designed for active lateral rotor vibration attenuation in cage induction electrical machines. We introduced a low-order parametric model for the actuator and identified it with a more detailed time-stepping FE method by using real machine data. In the modeling, we restricted to low-frequency vibratory phenomena neglecting the higher air-gap harmonics. Furthermore, linear equations were developed and the effect of saturation was included in the estimated parameters. The frequency responses from control winding input voltage to rotor displacement obtained from the simulations with FE time-stepping method indicate only a weak nonlinearity at the voltage range from 1 to 30 V. On the other hand, the FRFs from the disturbance force exerted on the rotor to the rotor center displacement show a considerable level of nonlinearity. This means that the disturbance force level (mass unbalance excitation) has to be estimated well in order to build a valid LTI model.

The simulation results predict that the force level achieved by the actuator is sufficient for active rotor vibration control. Also, the results predict that the low-order model is valid at low-frequency range at the vicinity of the rotation speed. This is a prerequisite when designing controllers for attenuation of rotor vibration primarily originating from the mass unbalance excitation at the rotor rotation speed [26,27].

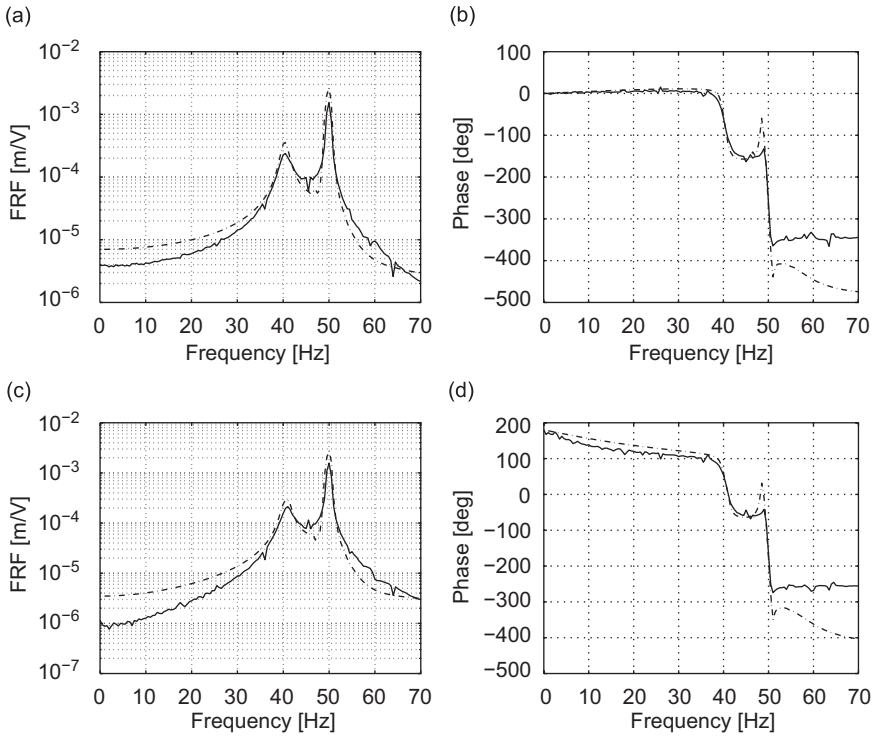

Fig. 14. Identification results of the actuator model from the control winding voltage to displacement: (a) first voltage component to horizontal displacement FRF magnitude, (b) first voltage component to horizontal displacement phase, (c) first voltage component to vertical displacement FRF magnitude and (d) first voltage component to vertical displacement phase. —, the simulated FRF; ---, the identified model FRF. The data was sampled at 1 kHz and the order of model was 10.

The simulation results indicate that the actuator has a sharp resonance at the supply frequency (50 Hz) of the motor. This may bring out some challenges for the control design. As a matter of fact, the direct force feedback is not achievable since the actuator force is not directly measurable. The control design with simulations and implementation to a laboratory-scale test machine belong to future research.

Acknowledgments

The authors gratefully acknowledge financial support from the Academy of Finland and VTT Technical Research Center of Finland. Special thanks are devoted to Dr. Slavomir Seman, ABB Drives, and Dr. Sami Kanerva, ABB Electrical Machines, for assistance with the system simulator. The authors want to thank Dr. Timo Holopainen, ABB Electrical Machines, for valuable discussions.

References

[1] J.S. Rao, *Vibratory Condition Monitoring of Machines*, Narosa Publishing House, New Delhi, India, 2000.

[2] M.D. Negrea, Electromagnetic Flux Monitoring for Detecting Faults in Electrical Machines, Doctoral Dissertation, Helsinki University of Technology, Department of Electrical and Communications Engineering, 2006, pp. 1–140, http://lib.tkk.fi/Diss/2006/isbn9512284774/.

[3] A. Chiba, T. Fukao, O. Ichikawa, M. Oshima, M. Takemoto, D.G. Dorrell, *Magnetic Bearings and Bearingless Drives*, Elsevier Newnes Press, Boston, MA, 2005.

[4] D. Dorrell, A. Smith, Calculation of u.m.p. in induction motors with series or parallel winding connections, *IEEE Transactions on Energy Conversion* 9 (2) (1994) 304–310.

[5] A. Smith, D. Dorrell, Calculation and measurement of unbalanced magnetic pull in cage induction motors with eccentric rotors, part i: analytical model, *Proceedings of the IEE Electric Power Applications* 143 (3) (1996) 193–201.

[6] D. Dorrell, A. Smith, Calculation and measurement of unbalanced magnetic pull in cage induction motors with eccentric rotors, part ii: experimental investigation, *Proceedings of the IEE Electric Power Applications* 143 (3) (1996) 202–210.
[7] F.D. Guo, D.C. Chu, The unbalanced magnetic pull and its effects on vibration in a three-phase generator with eccentric rotor, *Journal of Sound and Vibration* 254 (2) (2002) 297–312.
[8] K.-H. Ha, J.-P. Hong, Dynamic rotor eccentricity analysis by coupling electromagnetic and structural time stepping fem, *IEEE Transactions on Magnetics* 37 (5) (2001) 3452–3455.
[9] T.P. Holopainen, A. Tenhunen, A. Arkkio, Electromechanical interaction in rotordynamics of cage induction motors, *Journal of Sound and Vibration* 284 (3–5) (2005) 733–755.
[10] E. Rosenberg, Magnetic pull in electrical machines, *Transactions of the American Institute of Electrical Engineers* 37 (2) (1917) 1425–1469.
[11] A. Chiba, D.T. Power, M.A. Rahman, Characteristics of a bearingless induction motor, *IEEE Transactions on Magnetics* 27 (6) (1991) 5199–5201.
[12] A. Chiba, R. Furuichi, Y. Aikawa, K. Shimada, Y. Takamoto, T. Fukao, Stable operation of induction-type bearingless motors under loaded conditions, *IEEE Transactions on Industry Applications* 33 (4) (1997) 919–924.
[13] T. Hiromi, T. Katou, A. Chiba, M. Rahman, T. Fukao, A novel magnetic suspension-force compensation in bearingless induction-motor drive with squirrel-cage rotor, *IEEE Transactions on Industry Applications* 43 (1) (2007) 66–76.
[14] S. Watanabe, Vibration controller for rotating machine, Japanese Patent JP11027975.
[15] A. Chiba, T. Fukao, Optimal design of rotor circuits in induction type bearingless motors, *IEEE Transactions on Magnetics* 34 (4) (1998) 2108–2110.
[16] P.K. Kovács, *Transient Phenomena in Electrical Machines*, Elsevier Science Publishers, Amsterdam, 1984.
[17] T.P. Holopainen, A. Tenhunen, E. Lantto, A. Arkkio, Unbalanced magnetic pull induced by arbitrary eccentric motion of cage rotor in transient operation, Part 1: analytical model, *Electrical Engineering (Archiv für Electrotechnik)* 88 (1) (2005) 13–24.
[18] A. Arkkio, Analysis of induction motors based on the numerical solution of the magnetic field and circuit equations, *Acta Polytechnica Scandinavia, Electrical Engineering Series* 59 (1987) 1–97 http://lib.hut/Diss/list.html#1980.
[19] S. Kanerva, Simulation of Electrical Machines, Circuits and Control Systems Using Finite Element Method and System Simulator, Doctoral Dissertation, Helsinki University of Technology, Department of Electrical and Communications Engineering, 2005, pp. 1–92, http://lib.tkk.fi/Diss/2005/isbn9512276100/.
[20] P. van Overschee, B. DeMoor, *Subspace Identification of Linear Systems: Theory, Implementation, Applications*, Kluwer Academic Publishers, Dordrecht, 1996.
[21] G.J. Retter, *Matrix and Space-phasor Theory of Electrical Machines*, Akadémiai Kiadó, Budapest, 1987.
[22] R.R. Craig Jr., A review of time-domain and frequency-domain component mode synthesis method, *International Journal of Analytical and Experimental Modal Analysis* 2 (2) (1987) 59–72.
[23] A. Laiho, T.P. Holopainen, P. Klinge, A. Arkkio, Distributed model for electromechanical interaction in rotordynamics of cage rotor electrical machines, *Journal of Sound and Vibration* 302 (4–5) (2007) 683–698.
[24] G. Genta, *Vibration of Structures and Machines: Practical Aspects*, Springer, New York, 1999.
[25] A. Tenhunen, T.P. Holopainen, A. Arkkio, Spatial linearity of unbalanced magnetic pull in induction motors during eccentric rotor motions, *COMPEL: The International Journal for Computation and Mathematics in Electrical and Electronic Engineering* 22 (4) (2003) 862–876.
[26] C. Knospe, S. Fedigan, R.W. Hope, R. Williams, A multitasking dsp implementation of adaptive magnetic bearing control, *IEEE Transactions on Control Systems Technology* 5 (2) (1997) 230–238.
[27] K. Tammi, Active Control of Radial Rotor Vibrations: Identification, Feedback, Feedforward, and Repetitive Control Methods, Doctoral Dissertation, Department of Automation and Systems Technology, Helsinki University of Technology, 2007, pp. 1–165, http://lib.tkk.fi/Diss/2007/isbn9789513870089/.